



***HST*/COS Observations of Quasar Outflows in the 500–1050 Å Rest Frame. IV. The Largest Broad Absorption Line Acceleration**

Xinfeng Xu¹, Nahum Arav¹, Timothy Miller¹, Gerard A. Kriss², and Rachel Plesha²

¹ Department of Physics, Virginia Tech, Blacksburg, VA 24061, USA; xinfeng@vt.edu

² Space Telescope Science Institute, 3700 San Martin Drive, Baltimore, MD 21218, USA

Received 2019 June 27; revised 2019 September 20; accepted 2019 October 6; published 2020 March 16

Abstract

We present an analysis of the broad absorption line (BAL) velocity shift that appeared in one of the outflow systems in quasar SDSS J1042+1646. Observations were taken by the *Hubble Space Telescope*/Cosmic Origins Spectrograph in 2011 and 2017 in the 500–1050 Å rest frame. The outflow’s velocity centroid shifted by $\sim -1550 \text{ km s}^{-1}$ from $-19,500 \text{ km s}^{-1}$ to $-21,050 \text{ km s}^{-1}$ over a rest-frame time of 3.2 yr. The velocity shift signatures are most apparent in the absorption features from the Ne VIII $\lambda\lambda 770.41$ and 780.32 doublet and are supported by the absorption troughs from O V $\lambda 629.73$ and the Mg X $\lambda\lambda 609.79$ and 624.94 doublet. This is the first time where a quasar outflow velocity shift is observed in troughs from more than one ion and in distinct troughs from a doublet transition (Ne VIII). We attribute the velocity shift to an acceleration of an existing outflow as we are able to exclude photoionization changes and motion of material into and out of the line of sight as alternate explanations. This leads to an average acceleration of $480 \text{ km s}^{-1} \text{ yr}^{-1}$ (1.52 cm s^{-2}) in the quasar rest frame. Both the acceleration and the absolute velocity shift are the largest reported for a quasar outflow to date. Based on the absorption troughs of the O V* multiplet, we derive a range for the distance of the outflow (R) from the central source, $0.05 \text{ pc} < R < 54.3 \text{ pc}$. This outflow shows similarities with the fast X-ray outflow detected in quasar PG 1211+143. We use the acceleration and velocity shift to constrain radiatively accelerated active galactic nucleus disk–wind models and use them to make predictions for future observations.

Unified Astronomy Thesaurus concepts: Quasars (1319); Active galactic nuclei (16); Broad absorption line quasar (184); Active galaxies (17); Quasar absorption line spectroscopy (1317)

1. Introduction

Broad absorption line (BAL) outflows are seen in quasar spectra as wide, blueshifted absorption troughs (Weymann et al. 1991). These outflows can reach velocities up to $\approx 0.2c$ and have widths up to tens of thousands of km s^{-1} . The outflows provide important means of carrying energy and mass out of the quasar’s central region. Therefore, they likely participate in the interactions between the supermassive black holes (SMBHs) and their host galaxies (see elaboration in Section 1 of Arav et al. 2020, hereafter Paper I).

BAL troughs have been commonly observed to have variability on multi-year and shorter timescales, e.g., Filiz et al. (2013) reported that 50%–60% of C IV and Si IV BAL troughs were found to vary in their survey. However, reported cases of accelerating outflows are much rarer. Detections of BAL acceleration in individual objects have been known for two decades (e.g., Vilkoviskij & Irwin 2001; Hall et al. 2007). These studies reported that the outflow velocities shifted by up to $\sim 70 \text{ km s}^{-1}$ over rest-frame times of 1–5 yr and had an acceleration range between 0.03 and 0.15 cm s^{-2} . A velocity shift is measured directly from the spectra (e.g., from C IV absorption trough centroids) of two epochs, and the average acceleration is calculated by dividing this velocity shift by the quasar rest-frame time between the two epochs.

Surveys of BAL variability find no clear evidence for accelerating outflows (Gibson et al. 2008, 2010; Capellupo et al. 2012). The systematic investigation of C IV BAL acceleration/deceleration reported in Grier et al. (2016) shows a low detection rate of accelerating outflows (2 out of 140 quasars), where their two acceleration candidates show velocity shifts of up to $\sim 900 \text{ km s}^{-1}$ over rest-frame times of 3–5 yr.

Studies of BAL accelerations are challenging due to several reasons: (1) the need for long time baselines to observe the accumulated small acceleration signatures; (2) the difficulties in disentangling the velocity-dependent line profile changes from a true acceleration (Arav et al. 1999); and (3) the self-blending of BAL troughs (e.g., Arav et al. 2001; Scott et al. 2014).

Even though the observations of BAL acceleration are rare, they can provide valuable constraints on dynamical models of quasar outflows (e.g., Grier et al. 2016; Misawa et al. 2019), including: radiative driving (Murray et al. 1995), magnetic driving (Everett 2005), and thermal driving (Balsara & Krolik 1993).

In this paper, we present the discovery of a velocity shift for a BAL outflow seen in quasar SDSS J1042+1646. We attribute the velocity shift to an acceleration of an existing outflow as we are able to exclude photoionization changes and motion of material into and out of the line of sight (LOS) as alternate explanations (see Section 5.1). The structure of the paper is as follows. In Section 2, we discuss the observations and data. We present the evidence of the outflow velocity shift in Section 3. In Section 4, we show the photoionization analysis of the outflow. In Section 5, we discuss possible causes for the observed velocity shift and compare our results to previous studies. We also use the acceleration and velocity shift to constrain radiatively accelerated active galactic nucleus (AGN) disk–wind models in Section 5 and use them to make predictions for future observations. In Section 6, we summarize our results. We adopt a cosmology of $H_0 = 69.6 \text{ km s}^{-1} \text{ Mpc}^{-1}$, $\Omega_m = 0.286$, and $\Omega_\Lambda = 0.714$, and we use the Javascript Cosmology Calculator website (Wright 2006).

This paper is part of a series of publications describing the results of *Hubble Space Telescope* (HST) program GO-14777, which observed quasar outflows in the EUV500 using the Cosmic Origins Spectrograph (COS).

Paper I summarizes the results for the individual objects and discusses their importance to various aspects of quasar outflow research.

Paper II (Xu et al. 2020a) gives the full analysis for four outflows detected in SDSS J1042+1646, including the largest kinetic luminosity ($\dot{E}_k = 10^{47}$ erg s $^{-1}$) outflow measured to date at $R = 800$ pc and an outflow at $R = 15$ pc.

Paper III (Miller et al. 2020a) analyzes four outflows detected in 2MASS J1051+1247, which show remarkable similarities, are situated at $R \sim 200$ pc, and have a combined $\dot{E}_k = 10^{46}$ erg s $^{-1}$.

Paper IV is this work.

Paper V (Miller et al. 2020b) analyzes two outflows detected in PKS 0352-0711, including one outflow at $R = 500$ pc and a second outflow at $R = 10$ pc that shows an ionization-potential-dependent velocity shift for troughs from different ions.

Paper VI (Xu et al. 2020b) analyzes two outflows detected in SDSS 0755+2306, including one at $R = 220$ pc with $\dot{E}_k = 10^{46}$ erg s $^{-1}$.

Paper VII (T. R. Miller et al. 2020, in preparation) discusses the other objects observed by program GO-14777, whose outflow characteristics make the analysis more challenging.

2. Observations and Data Reduction

SDSS J1042+1646 (J2000: R.A. = 10:42:44.24, decl. = +16:46:56.14, $z = 0.978$) is 1 of 10 objects targeted by our HST program GO-14777 (PI: Arav; see Paper I). Observations were taken in 2017 November using the COS G130M and G160M gratings (Green et al. 2012). Previous observations were done at a roughly five times lower spectral resolution using the COS G140L grating in 2011 June. The wavelength calibrations of these gratings are described in Oliveira et al. (2010), where the specified 1σ wavelength error per exposure is 15 km s^{-1} for the G130M and G160M gratings and 150 km s^{-1} for the G140L grating. Empirically, the observed wavelength positions of the detected galactic interstellar medium (ISM) lines (including C II $\lambda 1334.53$, Fe II $\lambda 1608.45$, and Al II $\lambda 1670.79$) are in agreement between the two epochs to within 0.5 \AA ($\sim 120 \text{ km s}^{-1}$). For the G130M and G160M gratings, the detected ISM line positions are also consistent with the laboratory values within 0.03 \AA ($\sim 7 \text{ km s}^{-1}$). These wavelength errors are much smaller than the observed velocity shift (-1550 km s^{-1}) between the 2011 and 2017 epochs described in Section 3.

Detailed information about the observations and data reduction is given in Section 2 of Paper II, where a total of four outflow systems (S1–S4, see Table 1 here) were identified. The troughs from S1 show double-minima features, which are most apparent in the Na IX, Ar VII, and Ar VIII troughs (see Figure 3 of Paper II). Since these two features appear at the same velocity in several troughs, S1 is divided into two components, 1a and 1b. The four lower-velocity systems (S1a, S1b, S2, and S3) are consistent with no variations between the 2011 and 2017 epochs, and we report their analysis in Paper II. Here, we focus on the acceleration and physical characteristics of S4.

Table 1
Outflows Detected in the SDSS J1042+1646 Data

Outflow System	Velocity ^a (km s $^{-1}$)	Ne VIII Abs. Width ^b (km s $^{-1}$)
S1a	−4950	1700
S1b	−5750	1700
S2	−7500	1500
S3	−9940	1350
S4, 2011	−19500	2000
S4, 2017	−21050	2000

Notes.

^a The velocity centroids come from the Gaussian profile fitting to unblended absorption troughs, e.g., Ar VIII $\lambda\lambda 700.24, 713.80$.

^b Ne VIII $\lambda 770.41$ absorption trough width is measured for continuous absorption below a normalized flux of $I = 0.9$.

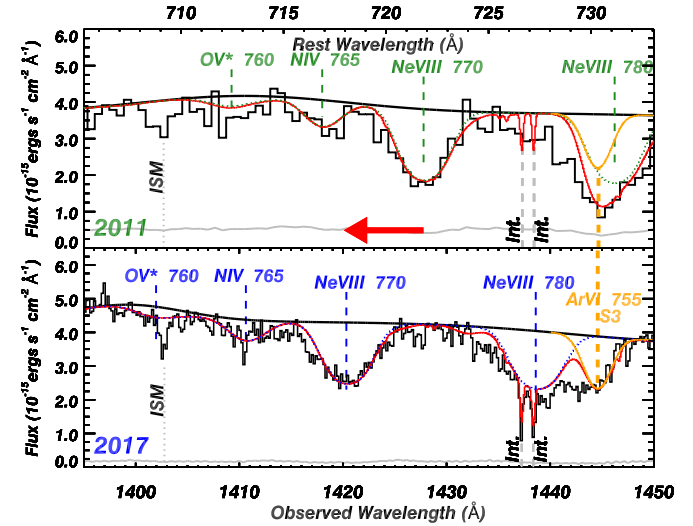


Figure 1. Velocity shift of the outflow S4 in SDSS J1042+1646. The top and bottom panels are for the 2011 and 2017 epochs, respectively. The data are shown as black histograms while the errors are shown as solid gray lines. We show the Gaussian fitting for the strong ionic absorption troughs in green and blue dotted lines for the 2011 and 2017 epochs, respectively (see details in Section 3.1). The absorption trough of Ar VI $\lambda 754.93$ from S3 is shown as the orange line in both panels (S3 does not vary between the two epochs). The combined absorption model in each panel is made by summing up all components and is shown as a solid red line. A strong Galactic ISM line (Si IV $\lambda 1402.77$) and intervening systems are marked by gray lines. The red arrow shows the direction and magnitude of the outflow shift from the 2011 to 2017 epoch.

3. Evidence for Outflow Velocity Shift

3.1. The Ne VIII Troughs

We present the 1395–1450 Å observed frame region in Figure 1, where the top and bottom panels are for the 2011 and 2017 epochs, respectively. The data are shown in black histograms, while the corresponding errors are shown as gray lines. The orange lines are the models for the Ar VI $\lambda 754.93$ absorption trough from outflow S3, which is a stable outflow with no observed variability (see Paper II). We observe deep absorption troughs from the Ne VIII doublet at 770.41 \AA and 780.32 \AA in both epochs. Since their optical depth ratios are close to unity, the troughs are saturated. The Ne VIII absorption trough widths are 2000 km s^{-1} for both the 2011 and 2017 epochs (see Table 1). Therefore, according to the BAL

definition for the EUV500 band discussed in Paper I, S4 is classified as a BAL outflow.

There is an apparent wavelength shift of the troughs for the Ne VIII doublet between the two epochs, as indicated by the red arrow. In order to identify this observed shift, we first fit the Ne VIII troughs in the 2017 epoch with Gaussian optical depth profiles. We fix their Gaussian velocity centroids at $-21,050 \text{ km s}^{-1}$, widths at $\sigma = 360 \text{ km s}^{-1}$, and depth ratio at 1:1. We scale their depths until the models fit the observed absorptions near 1420 \AA and 1438 \AA in the observed frame. These Gaussians are shown as the blue dotted lines on the bottom panel of Figure 1, and they fit the 2017 epoch's data well. We then apply the same Gaussian profiles (i.e., the same widths and depths) to the 2011 epoch but shift the velocity centroid to $-19,500 \text{ km s}^{-1}$. These Gaussians are shown as the green dotted lines on the top panel of Figure 1 and they fit well the troughs seen at 1428 \AA and 1445 \AA (observed frame). Both absorption features from the Ne VIII doublet have the same velocity shift (Δv) between the epochs and are well fitted with the same Gaussian width. These kinematic coincidences strongly suggest that we see the same outflow, but it has shifted by 1550 km s^{-1} during the six-yr interval between the two epochs (3.2 yr in the quasar rest frame).

3.2. Velocity Profiles Comparisons

To compare the velocity structure of the two epochs, Figure 2 shows the Ne VIII absorption troughs in velocity space. The top and bottom panels are for the 2011 and 2017 epochs, respectively. The x-axes of the 2011 and 2017 epochs are shown at the top and bottom, respectively, and are shifted by -1550 km s^{-1} . The blending from the Ar VI absorption trough of outflow S3 stays at the same velocity, and we mark the Ar VI velocity centroids with orange dashed lines. The velocity centroids of the Ne VIII doublet for the two epochs are $v_{c,2011} = -19,500 \text{ km s}^{-1}$ and $v_{c,2017} = -21,050 \text{ km s}^{-1}$ (marked with the black dotted lines).

In the top panel, the lower-velocity wings of the Ne VIII doublet troughs are similar, while the higher-velocity portion of the Ne VIII $\lambda 780.32$ is contaminated by the Ar VI $\lambda 754.93$ absorption trough of S3. Similarly, in the bottom panel, the higher-velocity wings of the Ne VIII doublet are nearly identical, while the lower-velocity portion of the Ne VIII $\lambda 780.32$ is contaminated by the stationary Ar VI $\lambda 754.93$ absorption trough of S3. These matches support the idea that the troughs we observed in both epochs come from the Ne VIII doublet transitions, which only partially cover the source and show non-black saturation.

In the middle panel of Figure 2, we compare the Ne VIII $\lambda 770.41$ absorption troughs between the two epochs, and it is evident that the two epochs' Ne VIII $\lambda 770.41$ troughs have nearly identical velocity structures when shifted by 1550 km s^{-1} . This strengthens the claim that the Ne VIII absorption troughs indeed shifted in velocity between 2011 and 2017 while the velocity profile remained unchanged.

3.3. Support from the Mg X and O V Troughs

The Synthetic Spectral Simulation (SSS) method creates a modeled spectrum based on the photoionization solution of the outflow (see Section 3.3 of Paper II and Section 4.1 here). In Figure 3, by using the photoionization solution derived in Section 4.1 (the red crosses in Figure 4), we show the spectral

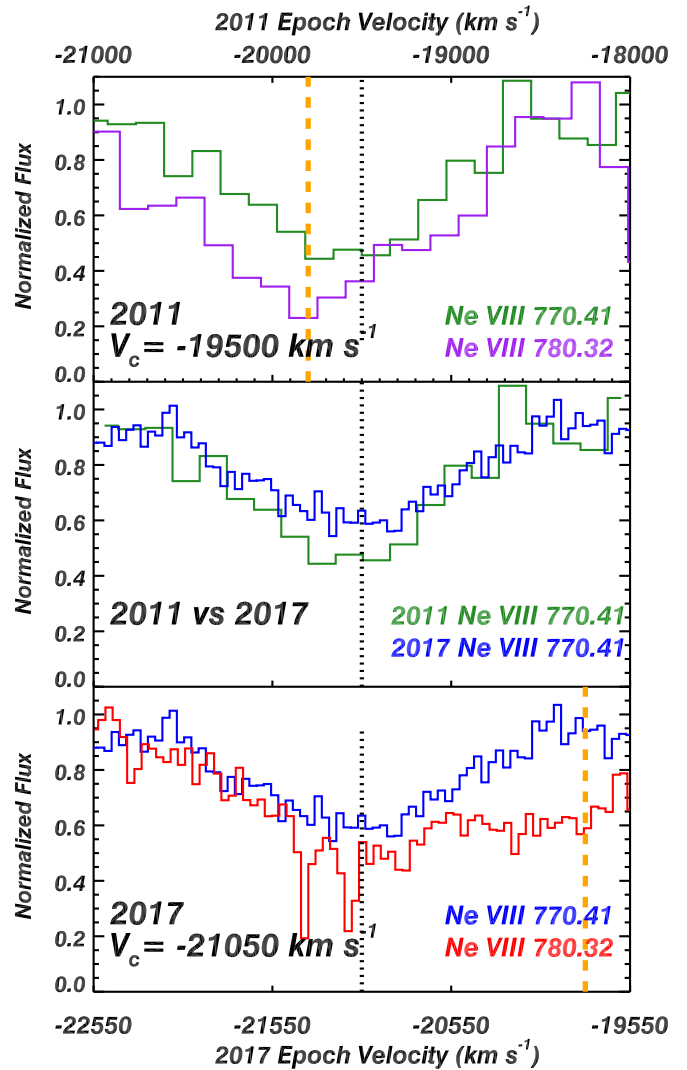


Figure 2. Comparison of the observed Ne VIII doublet absorption troughs between the 2011 and 2017 epochs. The velocity centroids (v_c) for each epoch are marked by the vertical, black dotted lines. The top and bottom panels' x-axes have a difference of -1550 km s^{-1} in order to align v_c for the 2011 and 2017 epochs. In the middle panel, we compare the Ne VIII $\lambda 770.41$ between the two epochs, where the 2011 trough is shifted by -1550 km s^{-1} (using the bottom velocity x-axis). The orange dashed lines point to the absorption troughs of Ar VI $\lambda 754.93$ from outflow S3 (see Section 3.1). The narrow intervening absorption systems seen in the 2017 observation in the Ne VIII $\lambda 780.32$ (at $\sim -21,100 \text{ km s}^{-1}$ and $21,300 \text{ km s}^{-1}$) are out of the velocity range in the top panel, which covers the $728\text{--}733 \text{ \AA}$ rest-frame region (see Figure 1).

region from about 1118 \AA to 1172 \AA (the observed frame), where we expect to observe the absorption troughs of Mg X $\lambda\lambda 609.79, 624.94$, and O V $\lambda 629.73$ from S4. The data and corresponding errors are shown as the black and gray histograms, respectively. Using Equations (2) and (3) from Paper II, we indicate the expected SSS model centroids of the absorption troughs for the 2011 and 2017 epochs in green and blue dashed lines, respectively. The absorption troughs of Ar VII $\lambda 585.75$ from outflow S1a and S1b do not vary between the two epochs, and we show both of them as the light-blue lines. Similarly for S3, the absorption troughs remain at the same velocity between the two epochs. We show them as purple solid lines (O IV $\lambda 608.40$ and O IV* $\lambda 609.83$) and a purple dotted line (Mg X $\lambda 609.79$). For the 2011 epoch, the

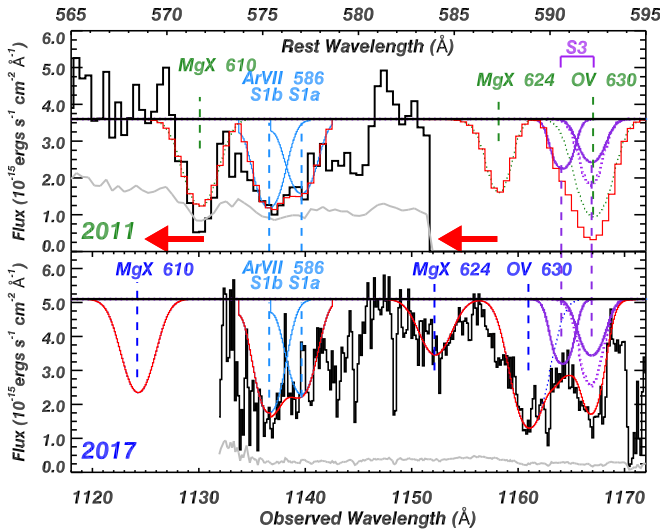


Figure 3. Spectral region for Mg X $\lambda\lambda 609.79$, 624.94 and O V $\lambda 629.73$ of S4 in SDSS J1042+1646. The labels and colors for S4 are the same as in Figure 1. The absorption troughs of Ar VII $\lambda 585.75$ from S1a and S1b are shown as the light-blue lines. The absorption troughs from S3 are shown as the purple solid lines (O IV $\lambda 608.40$ and O IV* $\lambda 609.83$) and purple dotted line (Mg X $\lambda 609.79$). S1a, S1b, and S3 did not vary between the two epochs. The red arrows show the direction and magnitude of the outflow shift from the 2011 to 2017 epoch. For S4, we identify the Mg X $\lambda 609.79$ trough of the 2011 epoch as well as the Mg X $\lambda 624.94$ and O V $\lambda 629.73$ troughs for the 2017 epoch. See the discussion in Section 3.3.

absorption troughs from O V $\lambda 629.73$ and Mg X $\lambda 624.94$ fall into the gap of the COS G140L grating (1152–1185 Å in the observed frame). The velocity centroid and width of the SSS model for the Mg X $\lambda 609.79$ trough are fixed. Therefore, the good fit of this modeled absorption to the trough seen at 1130 Å identifies the latter as the Mg X $\lambda 609.79$ trough of S4 in the 2011 epoch. Our 2017 model predicts a -1550 km s^{-1} shifted Mg X $\lambda 624.94$ trough that matches well with the absorption trough seen at 1152 Å (the observed frame). Mg X $\lambda 609.79$ and $\lambda 624.94$ are doublet transitions that arise from the same ion, and the wavelength separation between them is fixed. Therefore, observing similar troughs for Mg X $\lambda 609.79$ in the 2011 epoch and Mg X $\lambda 624.94$ in the 2017 epoch, shifted by -1550 km s^{-1} , is strong evidence that the outflow shifted in velocity over the six years.

Finally, the SSS model predicts an O V $\lambda 629.73$ trough consistent with the observed absorption near 1160 Å in the 2017 epoch. The combined absorption models (made by summing up all components) are shown as solid red lines in Figure 3.

3.4. Summary of Outflow Velocity Shift Evidence

The evidence for the velocity shift exhibited by outflow S4 is summarized as follows:

1. We identified in each epoch the Ne VIII $\lambda\lambda 770.41$ and 780.32 doublet troughs where the 2017 epoch's troughs are shifted by -1550 km s^{-1} (Section 3.1).
2. The kinematic similarity of these Ne VIII troughs secures their identification as arising from the Ne VIII doublet (Section 3.2).
3. The existence of troughs at the expected wavelength and velocity width for the Mg X $\lambda 609.79$ absorption in the 2011 epoch and Mg X $\lambda 624.94$ absorption in the 2017

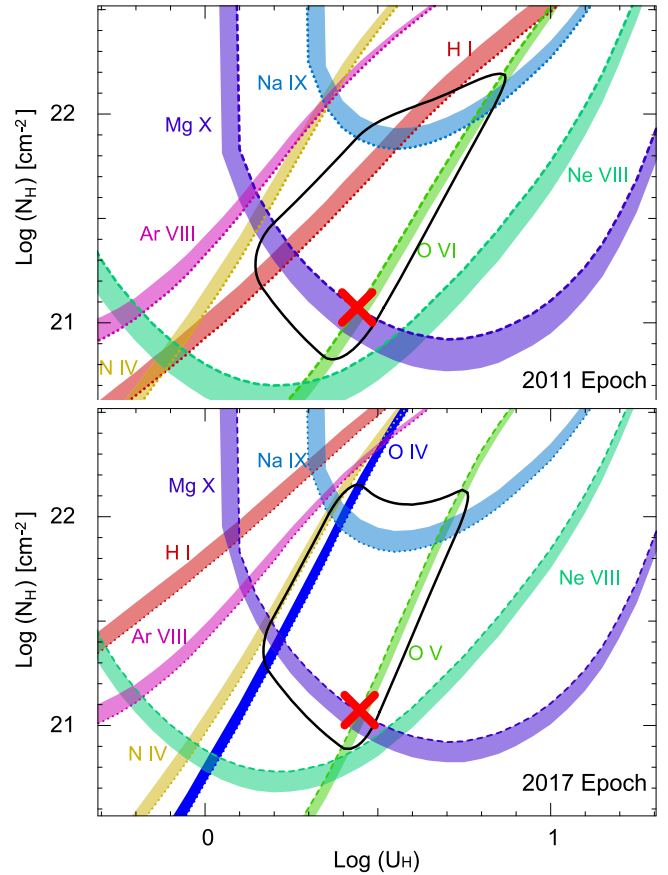


Figure 4. Photoionization solutions of outflow S4 for the 2011 and 2017 epochs. Each colored contour represents the region of N_{H} and U_{H} where the model predicts consistent N_{ion} with the observed ones within the errors. The dashed lines represent N_{ion} lower limits, which allow the phase spaces above the lines. The dotted lines represent N_{ion} upper limits, which allow the phase spaces below the lines. For each panel, the region within the black line is the allowed photoionization solution bounded by a 1σ error contour. The red crosses mark the adopted photoionization solutions for Figure 3.

epoch (-1550 km s^{-1} shifted compared to the 2011 epoch, Section 3.3).

4. The existence of a trough with the expected wavelength and shape of the predicted O V $\lambda 629.73$ trough in the 2017 epoch (Section 3.3).

4. Photoionization Analysis

4.1. Ionization Solution

The ionic column densities (N_{ion}) we measure are representative of the ionization structure for the outflowing material. With the aid of photoionization models, we can determine the physical characteristics of the outflow. We follow the SSS method in Paper II to derive the best fitting photoionization solution for both epochs separately. Here, we give a concise description of the SSS method (see the full discussion in Section 3.1 of Paper II).

1. We first measure the column densities (N_{ion}) from uncontaminated absorption troughs. Since there are no measurable doublet transitions in S4, we measure the N_{ion} of absorption troughs using the apparent optical depth method (AOD; see e.g., Savage & Sembach 1991). Adopting the same criteria as in Paper II, for singlet transitions with a maximum optical depth, τ_{max} , greater than 0.5, we treat the AOD N_{ion} as

Table 2
Column Densities for Outflow S4 in SDSS J1042+1646

Ion	λ^a (Å)	$N_{\text{ion, mea}}^b$ $\log(\text{cm}^{-2})$	$\frac{N_{\text{ion, mea}}}{N_{\text{ion, model}}}^c$
<i>Outflow System 4, 2011 epoch, $v = [-20800, -18600]^d$</i>			
H I	1025.72	<15.23	<3.39
N IV	765.15	<14.29	<29.5
O V	629.73	... ^d	...
O VI	1031.91	>16.08	>1.00
Ne VIII	770.41, 780.32	>15.98	>0.56
Na IX	694.15 ^e	<15.30	<6.3
Mg X	609.79	>15.73	>1.00
Ar VIII	700.24, 713.80	<14.46	<60.3
<i>Outflow System 4, 2017 epoch, $v = [-22150, -20000]^e$</i>			
H I	949.74	<16.10	<25.1
N IV	765.15	<14.20	<24.5
O IV	787.71	<14.59	<13.8
O V	629.73	>15.16	>1.00
O VI	1031.91, 1037.62	... ^f	...
Ne VIII	770.41, 780.32	>16.06	>0.68
Na IX	682.72	<15.30	<6.16
Mg X	624.94 ^f	>15.73	>1.00
Ar VIII	700.24	<14.56	<75.8

Note.

^a The rest wavelengths for the measured transitions. For doublet or multiplet transitions, we only show λ for measured troughs.

^b The measured column density (N_{ion}) for each ionic transition (see Section 4.1). Lower limits are shown in bold, while upper limits are shown in italics.

^c The measured N_{ion} divided by the model predicted N_{ion} .

^d The N_{ion} integration range in km s^{-1} .

^e O V $\lambda 629.73$, Na IX $\lambda 681.72$, and Mg X $\lambda 624.94$ fall into the gap of the COS G140L grating for the 2011 epoch (see Figure 3).

^f O VI $\lambda \lambda 1031.91, 1037.62$, and Mg X $\lambda 609.79$ are out of the observation range of the COS G130M grating for the 2017 epoch (see Figure 3).

lower limits. For absorption troughs with $\tau_{\text{max}} < 0.05$, we take the AOD N_{ion} as upper limits. None of the uncontaminated troughs have $0.05 < \tau_{\text{max}} < 0.5$. The measured N_{ion} are shown in Table 2.

2. A photoionization solution (PI₁) is built based on these measured N_{ion} . Photoionized plasma in a quasar outflow is characterized by the total hydrogen column density, N_{H} , and the ionization parameter, U_{H} , as

$$U_{\text{H}} = \frac{Q_{\text{H}}}{4\pi R^2 n_{\text{H}} c}, \quad (1)$$

where Q_{H} is the source emission rate of hydrogen ionizing photons, R is the distance of the outflow from the central engine, n_{H} is the hydrogen number density (for a highly ionized plasma, $n_{\text{e}} \simeq 1.2 n_{\text{H}}$), and c is the speed of light.

3. We run the spectral synthesis code Cloudy (version c17.00; Ferland et al. 2017) to generate grids of photoionization simulations. At each grid point, Cloudy predicts the N_{ion} for all ions in its database.

We assume a solar metallicity and adopt the spectral energy distribution (SED) of HE 0238 SED, which is based on the EUV500 observations of quasar HE 0238–1904 (Arav et al. 2013). We use the HE 0238 SED since: (a) for the observed data (the 570–1000 Å rest frame), the ratio of the HE 0238 SED

with respect to the SDSS J1042+1646 continuum is constant to within $\pm 10\%$; (b) the observation of quasar HE 0238–1904 has higher signal to noise; and (c) it allows us to compare the physical parameters of outflows from different objects with the same baseline SED. By integrating this SED, the bolometric luminosity of SDSS J1042+1646 is $\sim 1.5 \times 10^{47} \text{ erg s}^{-1}$.

We present the derived photoionization solutions for both epochs in Figure 4. The dashed lines represent N_{ion} lower limits, which allow the phase spaces above the lines. The dotted lines represent N_{ion} upper limits, which allow the phase spaces below the lines. For each ion, we add the measured N_{ion} error with an additional 20% error in quadrature (accounting for systematic errors, see Section 3.1 of Paper III), and treat this combined value as the final error. Since all N_{ion} are lower or upper limits, large regions in these phase spaces contain acceptable solutions, i.e., within the black contours. Both epochs show consistent solutions with $\log(N_{\text{H}})$ between 20.8 and 22.2 (hereafter, N_{H} is in units of $\log(\text{cm}^{-2})$) and $\log(U_{\text{H}})$ between 0.2 and 0.9. This consistency supports the claim that the outflow we observed in 2011 and 2017 are the same outflow, shifted by $1550_{-150}^{+150} \text{ km s}^{-1}$.

We also explored other SEDs (MF87, Mathews & Ferland 1987; UV-soft, Dunn et al. 2010) and metallicities (super solar, $Z = 4.67 Z_{\odot}$, described in Section 3.2 of Paper V). These choices change the $\log(U_{\text{H}})$ of the solution by less than 0.3 dex and lower $\log(N_{\text{H}})$ by up to 0.6 dex. The analysis of the velocity shift is not affected by these N_{H} and U_{H} differences.

4. We assume that all troughs in S4 can be modeled with similar Gaussian profiles (i.e., the same velocity centroid and width, see Equations (2) and (3) in Paper II). By adopting the predicted N_{ion} from Cloudy, we create an AOD synthetic spectrum model for the entire observed spectrum. In Figure 3, we show this synthetic spectrum using the photoionization solutions marked by the red crosses in Figure 4.

4.2. Determination of n_{e} from the O V* Multiplet

O V* has a multiplet of six transitions that create absorption troughs near 760 Å (the rest frame), and they are sensitive to a wide range of electron number densities (n_{e} ; see Section 4.2.3 in Paper II). We detect absorption at the expected wavelength locations of the O V* multiplet. We adopt the same analysis from Paper II as follows. Since the derived photoionization solutions allow large regions in the phase space (black contours in Figure 3), we check the photoionization solutions on the boundary of the contours and constrain n_{e} .

For the 207 epoch, we start with using the photoionization solution marked as the red cross in the bottom panel of Figure 3, and we adopt the model predicted value of $N(\text{O V})$ and the temperature. We vary $\log(n_{\text{e}})$ from 4 to 12 (hereafter, $\log(n_{\text{e}})$ is in units of cm^{-3}) and overlay the model predicted O V* troughs to the 1395–1415 Å observed frame region (see Figure 5). The red dashed lines represent the models of the O V* multiplet for a particular n_{e} , and the solid black lines are the summation of all models in this region. The model with $\log(n_{\text{e}}) = 6$ predicts minimal absorption troughs and clearly underestimates the observed trough, while the model with $\log(n_{\text{e}}) = 11$ overestimates the observations by more than 1σ . The absorption troughs are fitted well by the models with $\log(n_{\text{e}})$ between 9 to 10.5 for the 2017 epoch. We then do a similar analysis and constrain n_{e} , adopting different photoionization solutions on the boundary of the black contours in Figure 3. Combining all n_{e} constraints, we get

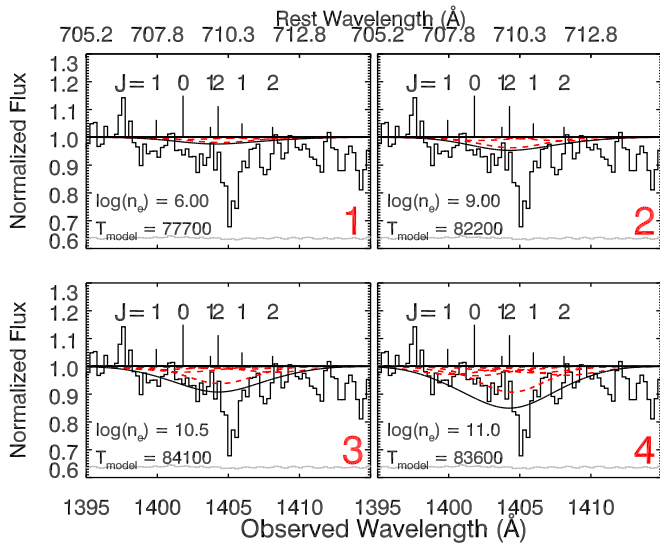


Figure 5. Fits to the O V* multiplet region for outflow S4. We vary n_e (in units of cm^{-3}) to get the best fit. The n_e and the corresponding temperature predicted from Cloudy are shown at the bottom-left corner of each panel. The black and gray solid histograms are the normalized flux and errors for the 2017 epoch. For each subplot, the red dashed lines represent the models of the O V* multiplet for a particular $\log(n_e)$, while the solid black lines are the summation of all models in this region. We start the y-axis from 0.6 to highlight the shallow O V* troughs, and we added 0.6 to the errors correspondingly. See Section 4.2 for a detailed discussion.

$4.5 < \log(n_e) < 10.5$. Incorporating this range with the derived photoionization solution, we constrain the distance (R) of this outflow in the range of $0.05 \text{ pc} < R < 54.3 \text{ pc}$.

The thickness of outflow S4 is $\Delta R = N_H/n_e < 0.01 \text{ pc}$. Therefore, the assumption that $\Delta R \ll R$ is valid and we can use Equations (6) and (7) in Borguet et al. (2012) to calculate the mass flow rate (\dot{M}) and kinetic luminosity (\dot{E}_k) of the outflow. The derived R values leads to a range of $0.07 M_\odot \text{ yr}^{-1} < \dot{M} < 141.5 M_\odot \text{ yr}^{-1}$ and $1.0 \times 10^{43} \text{ erg s}^{-1} < \dot{E}_k < 2.0 \times 10^{46} \text{ erg s}^{-1}$. For the 2011 epoch, the signal to noise and spectral resolution are lower, but the absorption troughs in the O V* region are consistent with the 2017 ones (see Figure 1). Caveat: this analysis is based on the assumption that most of the observed absorption in this region is from the O V* multiplet. If the observed absorption is not from O V*, we have the above derived n_e as an upper limit, $\log(n_e) < 10.5$, and R as a lower limit, $R > 0.05 \text{ pc}$.

5. Discussion

5.1. Excluding Other Explanations for the Shifted Troughs

The S4 outflow is a good candidate for an accelerating BAL outflow since the two epochs show not only similar velocity profiles but also close photoionization solutions. However, several other causes may explain the observed shift of the troughs:

1. Transverse motion of the outflowing material across the LOS (e.g., Moe et al. 2009; Capellupo et al. 2012; Yi et al. 2019). If this is the case, the BAL disappearance (the cloud moving out of the LOS) at $-19,500 \text{ km s}^{-1}$ and a new BAL appearance (the cloud moving into the LOS) at $-21,050 \text{ km s}^{-1}$ need to happen during the same 3.2 yr interval (the quasar rest-frame time). This is improbable since individually observed BAL appearance

and disappearance rates are low (2.3%–3.9%; Filiz et al. 2012; De Cicco et al. 2017; McGraw et al. 2017), where their observations span 0.3–4.9 yr rest-frame timescales.

2. Instrumental artifacts. We note that the 2011 epoch has a short exposure time ($\sim 900 \text{ s}$). In order to exclude any possible instrumental artifacts, we carefully looked at the data quality flags and calibration of the other observations taken close to our 2011 epoch observation. We found no possible instrumental issues that could significantly affect the region of interest (1395–1450 Å in the observed frame). We also checked the wavelength calibrations of both epochs as shown in Section 2.
3. Time-dependent photoionization changes. The idea is, instead of having one outflow that accelerated from $v_c = -19,500$ to $-21,050 \text{ km s}^{-1}$ between the 2011 and 2017 epochs, there are two stationary outflows, with one at each velocity. In this case, the changes in the absorption features between the two epochs are explained by changes in the incident ionizing flux of the quasar.

This quasar (SDSS J1042+1646) has four other outflows (S1a, S1b, S2, and S3), which have absorption troughs consistent with no variability between the 2011 and 2017 epochs. These include doublet troughs that are clearly not saturated (e.g., the Ar VIII $\lambda\lambda 700.24$ and 713.80 troughs in S2, see Figure 6 of Paper II). Significant changes in U_H would have caused large changes in these troughs, which are not detected. Therefore, the large U_H differences between the two epochs needed to explain the appearance and disappearance of the invoked S4 stationary outflows ($\Delta \log(U_H) \simeq 1.0$ dex, see a quantitative analysis below) are excluded.

We illustrate the possible photoionization change scenarios in Figure 6. We denote the photoionization solutions as $\text{PI}_{\alpha, \beta}$, where $\alpha = 11$ or 17 is for the 2011 and 2017 epochs, respectively, and $\beta = -v_{19}$ or $-v_{21}$ corresponds to the outflows at $v_c = -19,500 \text{ km s}^{-1}$ and $-21,050 \text{ km s}^{-1}$, respectively. In the top panel, we show the derived $\text{PI}_{11, v_{19}}$ (see Figure 4 and Section 4.1) as the black contour. Since we do not detect outflow troughs at $v = -21,050 \text{ km s}^{-1}$ in the 2011 epoch, we overlay in the top panel the measured N_{ion} upper limits for the v_{21} outflow from the 2011 epoch (colored dotted lines with corresponding 1σ error contours). Similarly, in the bottom panel, we show the derived $\text{PI}_{17, v_{21}}$ as the black contour and N_{ion} upper limits for the v_{19} outflow measured from the 2017 epoch as colored dotted lines (with corresponding 1σ error contours).

We assume that the N_H for each outflow did not change significantly between the two epochs. Otherwise, we are in the regime of the transverse motion scenario, which we showed was improbable in point (1) above. We now ask the question: at what U_H values would the v_{21} outflow be consistent with the N_{ion} upper limits of the 2011 epoch? To answer that, we take the (N_H, U_H) solution of the v_{21} outflow from the 2017 epoch (the black contour on the bottom panel of Figure 6) and superimpose it on the top panel. To match the N_{ion} constraints, we are allowed to change only U_H as N_H is assumed constant. The minimal U_H shift is shown by the position of the red contour in the top panel. Therefore, we can match the N_{ion} constraints for the v_{21} outflow from the 2011 epoch if U_H of the v_{21} outflow from the 2017 epoch increases by at least $\Delta \log(U_H)_I = 1.0$ dex (shown as the solid red arrow).

Since the quasar is the only ionizing photon source, $\text{PI}_{17, v_{19}}$ would have the same magnitude of U_H shift with respect to

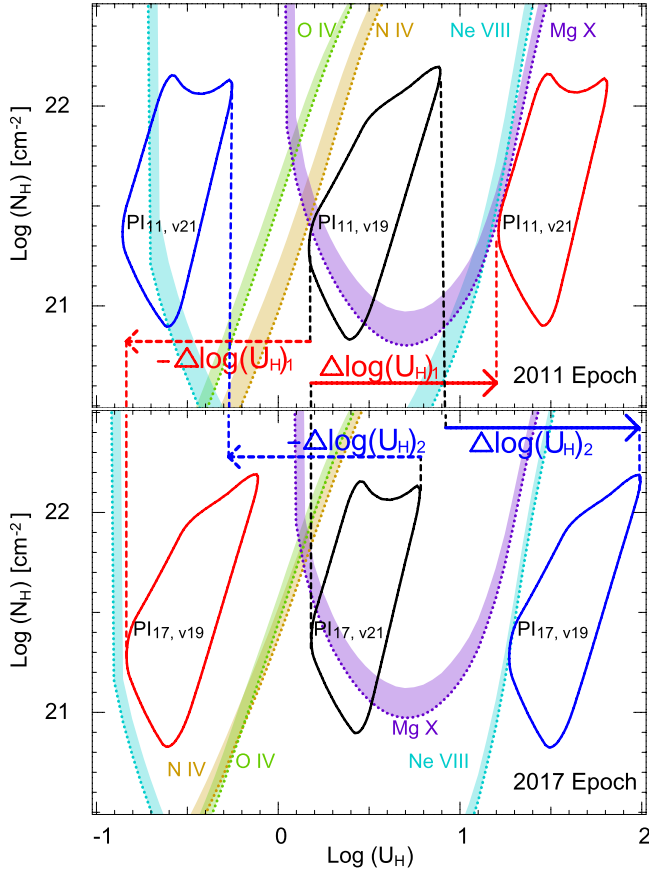


Figure 6. Phase plot for demonstrating the inability of a time-dependent photoionization model to explain the observed troughs of outflow S4. Top: for the 2011 epoch, we show the derived photoionization solution of the outflow centered at $v_c = -19,500 \text{ km s}^{-1}$ (v19, see Section 4.1) as the black contour and the measured N_{ion} upper limits for the $v_c = -21,050 \text{ km s}^{-1}$ (v21) outflow as the color dotted lines with their 1σ error contours. Bottom: for the 2017 epoch, we show the derived photoionization solution of the outflow centered at $v_c = -21,050 \text{ km s}^{-1}$ as the black contour and the measured N_{ion} upper limits for the $v_c = -19,500 \text{ km s}^{-1}$ outflow as the color dotted lines. The minimal U_H for a stationary v21 outflow in 2011 (red oval, top panel) predicts the red oval N_H/U_H solution for the v19 component in 2017. The latter is excluded by the measured column density upper limits of N IV, O IV, and Ne VIII. Similarly, a high U_H solution for the v19 outflow in 2017 (blue oval, bottom panel) is excluded by the predicted 2011 N_H/U_H solution of the v21 component (blue oval, top panel). See an elaboration in Section 5.1.

PI_{11, v19} but in the opposite direction ($-\Delta \log(U_H)_1$ and the dashed red arrow), and the corresponding PI_{17, v19} is shown as the red contour in the bottom panel. We find that all (U_H, N_H) solutions within PI_{17, v19} overestimate the measured N_{ion} upper limits of N IV and O IV in the 2017 epoch by at least an order of magnitude. Thus, this is not a viable scenario.

Similarly, in the bottom panel, we do not detect outflow troughs from the v19 system in the 2017 epoch. We take the $(N_H \text{ and } U_H)$ solution of the v19 outflow from the 2011 epoch (the black contour on the top panel), and superimpose it on the bottom panel to match the measured N_{ion} upper limits here. This corresponds to a U_H shift between PI_{17, v19} (the blue contour in the bottom panel) and PI_{11, v19} (the black contour in the top panel) of $\Delta \log(U_H)_2 > 1.1$ dex, with the minimum shift marked as the solid blue arrow. PI_{11, v21} would have the same magnitude as a U_H shift with respect to PI_{17, v21} but in the

Table 3
Comparisons of BAL Acceleration Candidates

References	Δt_{rest}^a (yr)	Δv (km s^{-1})	Accel. ^b (cm s^{-2})	Accel. ^b ($\text{km s}^{-1} \text{ yr}^{-1}$)
Vilkoviskij & Irwin (2001)	5.0	55	$0.035^{+0.016}_{-0.016}$	11^{+5}_{-5}
Hall et al. (2007)	1.4	70	$0.15^{+0.025}_{-0.025}$	50^{+8}_{-8}
Grier et al. (2016) ^c	3.7	730	$0.63^{+0.14}_{-0.12}$	200^{+44}_{-38}
Grier et al. (2016) ^c	5.2	890	$0.54^{+0.04}_{-0.04}$	170^{+13}_{-13}
This work	3.2	1550	$1.52^{+0.16}_{-0.16}$	480^{+50}_{-50}

Notes.

^a The time intervals measured in the quasar rest frame.

^b The average acceleration measured in the quasar rest frame.

^c Grier et al. (2016) reported two BAL acceleration candidates.

opposite direction ($-\Delta \log(U_H)_2$ and the dashed blue arrow). Again, we find that all $(U_H \text{ and } N_H)$ solutions within PI_{11, v21} (the blue contour at the top panel) violate the measured N_{ion} upper limits of N IV and O IV in the 2011 epoch by at least 1.1 dex, eliminating the validity of this scenario.

There are two additional concerns regarding the time-dependent photoionization, which need to be discussed.

(a) Since v19 and v21 could be at different R with respect to the central quasar, the inner outflow responds earlier to the change in ionizing flux than the outer outflow. However, since both outflows are observed in the LOS, the response of the inner outflow propagates toward us at the speed of light and coincides with the observed response of the outer outflow. Therefore, from our perspective, both outflows react to the change in the ionizing flux of the quasar simultaneously.

(b) The reaction time for the outflows to reach photoionization equilibrium when the ionizing flux from the quasar changes. Both outflows have an electron number density (n_e) in the range of $10^{4.5} - 10^{10.5} \text{ cm}^{-3}$ (see Section 4.2). When U_H decreases or increases by 1 dex, the response time for an ionic transition like Ne VIII in outflows with these n_e values is $\lesssim 10$ days (e.g., Krolik & Kriss 1995). From statistical studies of quasar variabilities (e.g., Filiz et al. 2013; De Cicco et al. 2017), BAL quasar outflows barely vary for a rest-frame timescale of < 1 yr. Thus, both v19 and v21 outflows are likely in photoionization equilibrium when observed. These two points do not affect our exclusion of the photoionization change scenario above.

Overall, we exclude the motion of material into and out of the LOS, instrumental artifacts, and time-dependent photoionization changes as alternate explanations. Therefore, the outflow acceleration scenario is the only viable physical cause for the observed -1550 km s^{-1} velocity shift in S4.

5.2. Comparisons with Other Studies

As mentioned in Section 1, there are a few prior studies on BAL accelerations. In Table 3, we summarize and compare them to our findings. We report the observed velocity shift in the third column, which is measured directly from the spectra. In the fourth and fifth columns, we report the average acceleration in the quasar's rest frame in two units, cm s^{-2} and $\text{km s}^{-1} \text{ yr}^{-1}$. We note that the S4 outflow not only has the largest velocity shift observed to date, i.e., 1550 km s^{-1} ; but also has the largest BAL acceleration observed to date, i.e.,

Table 4
Comparisons of Outflow Parameters to Quasar PG 1211+143

Outflow	v (km s ⁻¹)	$\log(N_{\text{H}})$ (log(cm ⁻²))	$\log(U_{\text{H}})$
SDSS J1042+1646, S4	-21,000	20.8–22.2	0.2–0.9
PG 1211+143	-17,000	21.5	1.6

$480_{-50}^{+50} \text{ km s}^{-1} \text{ yr}^{-1} = 1.52_{-0.16}^{+0.16} \text{ cm s}^{-2}$ in the quasar rest frame.

The previous studies of BAL acceleration in Table 3 detected a velocity shift only in the C IV $\lambda\lambda 1548.19$ and 1550.77 absorption trough where, for BAL outflows, the absorption troughs from the C IV doublet usually blend together (e.g., Grier et al. 2016). For S4, a consistent velocity shift signature is detected in four troughs, which is the first time that a quasar outflow velocity shift is observed from more than one ion and in distinct troughs from a doublet transition (Ne VIII, see Section 3).

5.3. Similarity with the PG 1211+143 X-Ray Outflow

Outflow S4 has a similar velocity to the X-ray outflow seen in PG 1211+143 ($-17,300 \text{ km s}^{-1}$). The latter is the only high-velocity outflow detected in X-ray grating spectra, which includes troughs from Ne X–Ly α , Mg XII–Ly α , Si XIII–He α , and Si XIV–Ly α using *Chandra* observations (Danekhar et al. 2018; see also Pounds et al. 2016a, 2016b for detection of similar troughs using *X-ray Multi-Mirror Mission (XMM-Newton)* Reflection Grating Spectrometer (RGS) data). This X-ray absorber in PG 1211+143 is well fitted with $\log(N_{\text{H}}) \sim 21.5$ and $\log(\xi) \sim 2.9$, where ξ is the X-ray ionization parameter. For the HE 0238 SED, we have the relation: $\log(U_{\text{H}}) = \log(\xi) - 1.3$. The ultraviolet counterpart of this X-ray outflow has been detected in *HST*/COS observations, which yields a broad Ly α absorption feature at $v = -17,000 \text{ km s}^{-1}$ ($-0.056c$; Kriss et al. 2018). We compare the v , N_{H} , and U_{H} values between the X-ray outflow in PG 1211+143 and outflow S4 in Table 4.

We conclude that our observations in the EUV500 band have probed an outflow with similar velocity and N_{H} to the one observed in PG 1211+143. The U_{H} value of the PG 1211+143 ($\log(U_{\text{H}}) = 1.6$) is roughly an order of magnitude larger than what we find for S4, using the EUV500 data. This suggests that S4 may have an even higher ionization phase similar to the one in PG 1211+143, which could be detected by future X-ray observatories (e.g., *Athena*, Barcons et al. 2017).

5.4. BAL Acceleration and the Disk-Wind Model

Radiatively accelerated disk-wind models (e.g., Arav & Begelman 1992; Murray et al. 1995; Proga 2003; Proga & Kallman 2004) are possible explanations for the origin of the observed BAL outflow. As shown in Equation (7) of Murray et al. (1995), for a radiatively accelerated outflow, the radial velocity has the form:

$$v(r) = v_{\infty}(1 - r_f/r)^{\beta}, \quad (2)$$

where $v(r)$ is the observed outflow velocity, r_f is the launching radius of the outflow, r is the outflow's current radius, and $\beta \sim 1.15$ (the full range of 1.1–1.2 from Murray & Chiang 1997).

Table 5
Predictions for BAL Accelerations in SDSS J1042+1646 (S4)

Epoch	Δv^a (km s ⁻¹)	v^b (km s ⁻¹)	a^c (cm s ⁻²)	a^c (km s ⁻¹ yr ⁻¹)	r^d (pc)
2017 ^e	0	21050	1.52	480	0.23
2019	400	21400	1.31	410	0.25
2022	800	21900	1.06	330	0.28
2027	1500	22500	0.76	240	0.34

Note.

^a The velocity difference of S4 between the predicted time and the 2017 epoch.

^b Predicted outflow velocity of S4.

^c Predicted acceleration of S4 in the quasar's rest frame.

^d Predicted outflow distance of S4 to the quasar.

^e We show the measured parameters for the 2017 epoch as a comparison.

The corresponding acceleration derived from Equation (2) is

$$a(r) \equiv \frac{dv}{dt} \equiv v \frac{dv}{dr} = 1.15 \frac{v_{\infty}^2 r_f}{r^2} \left(1 - \frac{r_f}{r}\right)^{1.30}. \quad (3)$$

If the outflow is accelerated by radiation pressure, we have the terminal velocity of the outflow as

$$v_{\infty} = F \sqrt{GM/r_f}, \quad (4)$$

where M is the central black hole's mass, G is the gravitational constant, and F is scaling factor (~ 1.5 – 3.5 ; Murray et al. 1995; Laor & Brandt 2002; Baskin et al. 2014). Using Equation (4), Equations (2) and (3) can be rewritten as

$$v(r) = F \sqrt{GM/r_f} \left(1 - \frac{r_f}{r}\right)^{1.15} \quad (5)$$

and

$$a(r) = 1.15 \frac{F^2 GM}{r^2} \left(1 - \frac{r_f}{r}\right)^{1.30}. \quad (6)$$

In our case, $v(r) = 21,050 \text{ km s}^{-1}$ and $a(r) = 1.52 \text{ cm s}^{-2}$ are derived from the velocity shift between the 2011 and 2017 epochs (see Section 3). The Sloan Digital Sky Survey (SDSS) spectrum of J1042+1646 shows a Mg II broad emission line (BEL). By fitting this BEL using the Mg II–based black hole mass estimators (see Equation (7) and Table 4 in Bahk et al. 2019), we derived $M \sim 2.0 \times 10^9 M_{\odot}$. The unknowns in Equations (4)–(6) are F , r , and r_f . As shown in Section 4.1 of Grier et al. (2016), the disk-wind model of Murray & Chiang (1997) will be viable if these equations are satisfied by the observations. To solve these equations, we vary F between 1.5 and 3.5, and r/r_f between 1 and 100, both in steps of 0.1. We find a good solution when $F = 1.8$ and $r/r_f = 5.7$. With these values of F and r/r_f , the model predicts that the launching radius is $r_f \sim 1.2 \times 10^{15} \text{ m}$ (0.04 pc); the observing radius is 5.7 times r_f , i.e., $r \sim 0.23 \text{ pc}$; and the terminal velocity is $v_{\infty} \sim 26,000 \text{ km s}^{-1}$.

Only with additional epochs will we be able to test if the above solution predicts the correct $v(r)$ and $a(r)$ for the outflow. Based on the above derived outflow parameters, we integrate Equation (5) and predict the accelerations of S4 for the next 2, 5, and 10 yr in the observed frame (see Table 5). Under the disk-wind model, the outflow's acceleration decreases by $\sim 40\%$ and the velocity reaches $\sim 22,500 \text{ km s}^{-1}$ in 10 yr. These results are similar to the BAL outflow acceleration reported in Grier et al. (2016). They observed C IV BAL

accelerations between three epochs for quasar SDSS J0124–0033. The observed average acceleration dropped from 0.90 cm s^{-2} between epochs 1 and 2 to 0.37 cm s^{-2} between epochs 2 and 3. However, they found that the disk–wind model is insufficient to explain their observations since the parameters derived from their epochs 1 and 2 overpredict the velocity shift by about a factor of five when applied to epoch 3.

Similarly, additional *HST*/COS observations of quasar SDSS J1042+1646 in the next decade will be able to test the prediction of the radiatively-driven disk–wind model (see Table 5). In addition, for outflow S4, we have distance constraints (see Section 4.2). Therefore, contrasting the model predictions with the r , v , and a extracted from future observations will be particularly instructive for testing and understanding the acceleration mechanisms of quasar outflows.

6. Summary

In this paper, we identified and analyzed the BAL acceleration for outflow S4 in quasar SDSS J1042+1646. The main results are summarized as follows:

1. We observed significant velocity shift signatures in multiple ionic absorption troughs for outflow system 4. The Ne VIII absorption troughs show similar velocity structures over the six-yr interval (see Section 3), while the trough centroids shifted by -1550 km s^{-1} over 3.2 yr in the quasar rest frame. Moreover, for both the 2011 and 2017 epochs, we obtained the photoionization models using the SSS method and the photoionization solutions are similar for the two epochs (see Section 4.1). These two points support the claim that we observe the same outflow but it is shifted by -1550 km s^{-1} .
2. We attribute the velocity shift to acceleration since we are able to exclude time-dependent photoionization changes and motion of material into and out of the LOS as alternate explanations (see Section 5.1). This leads to an average acceleration of $480_{-50}^{+50} \text{ km s}^{-1} \text{ yr}^{-1}$ or $1.52_{-0.16}^{+0.16} \text{ cm s}^{-2}$.
3. We compared our results with previous studies of BAL accelerations and concluded that the S4 outflow has the largest velocity shift and acceleration observed in BAL outflows to date (see Section 5.2). This is also the first time where quasar outflow acceleration is observed from more than one ion and in distinct troughs from a doublet transition (Ne VIII, see Section 3).
4. The outflow velocity and N_{H} are similar to the high-velocity X-ray outflow reported in PG 1211+143, which suggest that we probe similar outflows in both cases (see Section 5.3).
5. Using the observed velocities and associated acceleration, the disk–wind model of Murray & Chiang (1997) yields $R = 0.23 \text{ pc}$ for outflow S4. We also have distance constraints derived from the O V^* multiplet ($0.05 \text{ pc} < R < 54.3 \text{ pc}$, see Section 4.2). The disk–wind model makes predictions for future values of v , a , and r (see Table 5), which can be uniquely tested with future *HST*/COS observations (see Section 5.4).

X.X., N.A., and T.M acknowledge support from NSF grant AST 1413319, as well as NASA STScI grants GO 14777, 14242, 14054, and 14176, and NASA ADAP 48020.

Based on observations made with the NASA/ESA *Hubble Space Telescope*, and obtained from the data archive at the Space Telescope Science Institute. STScI is operated by the Association of Universities for Research in Astronomy, Inc. under NASA contract NAS5-26555.

ORCID iDs

Xinfeng Xu  <https://orcid.org/0000-0002-9217-7051>

Timothy Miller  <https://orcid.org/0000-0002-0730-2322>

Gerard A. Kriss  <https://orcid.org/0000-0002-2180-8266>

References

- Arav, N., & Begelman, M. C. 1992, *ApJ*, **401**, 125
- Arav, N., Borguet, B., Chamberlain, C., Edmonds, D., & Danforth, C. 2013, *MNRAS*, **436**, 3286
- Arav, N., Brotherton, M. S., Becker, R. H., et al. 2001, *ApJ*, **546**, 140
- Arav, N., Korista, K. T., de Kool, M., Junkkarinen, V. T., & Begelman, M. C. 1999, *ApJ*, **516**, 27
- Arav, N., Xu, X., Miller, T., Kriss, G. A., & Plesha, R. 2020, *ApJS*, **247**, 37
- Bahk, H., Woo, J.-H., & Park, D. 2019, *ApJ*, **875**, 50
- Balsara, D. S., & Krolik, J. H. 1993, *ApJ*, **402**, 109
- Barcons, X., Barret, D., Decourchelle, A., et al. 2017, *AN*, **338**, 153
- Baskin, A., Laor, A., & Stern, J. 2014, *MNRAS*, **445**, 3025
- Borguet, B. C. J., Edmonds, D., Arav, N., Dunn, J., & Kriss, G. A. 2012, *ApJ*, **751**, 107
- Capellupo, D. M., Hamann, F., Shields, J. C., Rodríguez Hidalgo, P., & Barlow, T. A. 2012, *MNRAS*, **422**, 3249
- Danehar, A., Nowak, M. A., Lee, J. C., et al. 2018, *ApJ*, **853**, 165
- Filiz, Ak, N., Brandt, W. N., Grier, C. J., & Paolillo, M. 2017, *FrASS*, **4**, 64
- Dunn, J. P., Bautista, M., Arav, N., et al. 2010, *ApJ*, **709**, 611
- Everett, J. E. 2005, *ApJ*, **631**, 689
- Ferland, G. J., Chatzikos, M., Guzman, F., et al. 2017, *RMxAA*, **53**, 385
- Filiz, Ak, N., Brandt, W. N., Hall, P. B., et al. 2012, *ApJ*, **757**, 114
- Filiz, Ak, N., Brandt, W. N., Hall, P. B., et al. 2013, *ApJ*, **777**, 168
- Gibson, R. R., Brandt, W. N., Gallagher, S. C., Hewett, P. C., & Schneider, D. P. 2010, *ApJ*, **713**, 220
- Gibson, R. R., Brandt, W. N., Schneider, D. P., & Gallagher, S. C. 2008, *ApJ*, **675**, 985
- Green, J. C., Froning, C. S., Osterman, S., et al. 2012, *ApJ*, **744**, 60
- Grier, C. J., Brandt, W. N., Hall, P. B., et al. 2016, *ApJ*, **824**, 130
- Hall, P. B., Sadavoy, S. I., Hutsemekers, D., Everett, J. E., & Rafiee, A. 2007, *ApJ*, **665**, 174
- Kriss, G. A., Lee, J. C., Danehar, A., et al. 2018, *ApJ*, **853**, 166
- Krolik, J. H., & Kriss, G. A. 1995, *ApJ*, **447**, 512
- Laor, A., & Brandt, W. N. 2002, *ApJ*, **569**, 641
- Mathews, W. G., & Ferland, G. J. 1987, *ApJ*, **323**, 456
- McGraw, S. M., Brandt, W. N., Crier, C. J., et al. 2017, *MNRAS*, **469**, 3163
- Miller, T. R., Arav, N., Xu, X., Kriss, G. A., & Plesha, R. 2020a, *ApJS*, **247**, 39
- Miller, T. R., Arav, N., Xu, X., Kriss, G. A., & Plesha, R. 2020b, *ApJS*, **247**, 41
- Misawa, T., Eracleous, M., Charlton, J. C., & Kashikawa, N. 2019, *ApJ*, **870**, 68
- Moe, M., Arav, N., Bautista, M. A., & Korista, K. T. 2009, *ApJ*, **706**, 525
- Murray, N., & Chiang, J. 1997, *ApJ*, **474**, 91
- Murray, N., Chiang, J., Grossman, S. A., & Voit, G. M. 1995, *ApJ*, **451**, 498
- Oliveira, C., Béland, S., Keyes, C., & Niemi, S. 2010, SMOV: COS FUV Wavelength Calibration COS Instrument Sci. Rep. 2010-06(v1), Baltimore, MD: STScI http://www.stsci.edu/hst/cos/documents/isrs/ISR2010_06.pdf
- Pounds, K. A., Lobban, A., Reeves, J. N., & Vaughan, S. 2016a, *AN*, **337**, 518
- Pounds, K. A., Lobban, A., Reeves, J. N., Vaughan, S., & Costa, M. 2016b, *MNRAS*, **459**, 4389
- Proga, D. 2003, *ApJL*, **592**, L9
- Proga, D., & Kallman, T. R. 2004, *ApJ*, **616**, 688
- Savage, B. D., & Sembach, K. R. 1991, *ApJ*, **379**, 245
- Scott, A. E., Brandt, W. N., Behar, E., et al. 2014, *ApJ*, **797**, 105
- Vilkovskij, E. Y., & Irwin, M. J. 2001, *MNRAS*, **321**, 4
- Weymann, R. J., Morris, S. L., Foltz, C. B., & Hewett, P. C. 1991, *ApJ*, **373**, 23
- Wright, E. L. 2006, *PASP*, **118**, 1711
- Xu, X., Arav, N., Miller, T., Kriss, G. A., & Plesha, R. 2020a, *ApJS*, **247**, 38
- Xu, X., Arav, N., Miller, T., Kriss, G. A., & Plesha, R. 2020b, *ApJS*, **247**, 42
- Yi, W., Brandt, W. N., Hall, P. B., et al. 2019, *ApJS*, **242**, 28